Global Biogeochemical Cycles

Supporting Information for

Amplified subsurface signals of ocean acidification

Andrea J. Fassbender[1,*], Brendan R. Carter[2,1], Jonathan D. Sharp[2,1], Yibin Huang[4,3,1], Mar C. Arroyo[3,1], Hartmut Frenzel[2,1]

[1]NOAA/OAR Pacific Marine Environmental Laboratory, Seattle, WA, 98115
[2]Cooperative Institute for Climate, Ocean, and Ecosystem Studies, University of Washington, Seattle, WA, 98195
[3]Department of Ocean Sciences, University of California Santa Cruz, Santa Cruz, CA, 95064
[4]Cooperative Institute for Marine and Atmospheric Research, University of Hawai'i at Manoa, Honolulu, HI, 96822

[*]Andrea J. Fassbender
Email: andrea.j.fassbender@noaa.gov

Contents of this file

Text S1 to S4

Figures S1 to S20

References

Text S1: ***Sensitivity of nonlinearity results to the respiratory quotient***

While use of the canonical respiratory quotient (O_2:C = -170/117) in our study may be appropriate for evaluating the bulk remineralized carbon pool in the ocean interior, it differs significantly from in situ respiratory quotient estimates primarily made at the sea surface, regionally, and over short timescales that provide mixed evidence for latitudinal variability (Henderikx Freitas et al., 2020; Moreno et al., 2020, 2022). Any bias or spatial variability in the respiratory quotient would influence the fraction of total carbon attributed to the regenerated versus preformed carbon pool. This in turn would impact the magnitude of OA metric changes attributed to nonlinear carbonate chemistry effects induced by natural and anthropogenic carbon pool interactions. To test the sensitivity of our results to the respiratory quotient, we repeated the nonlinearity calculations using respiratory quotients that were 30% larger and 30% smaller than the canonical value. As expected, the component of C_{ant}-driven OA metric changes attributed to nonlinear carbonate chemistry effect scales with the respiratory quotient (**Figures S9-S10**). However, the large-scale spatial patterns and primary takeaways of our analysis are robust to changes in the canonical respiratory quotient of at least ±30%.

Text S2: ***Validation of nonlinearity results derived from combining two mapped data products***

Combining the Carter et al. (2021) preformed properties mapped product with the GLODAPv2.2016b mapped product to evaluate the influence of carbonate system nonlinearities should provide coherent results since the development of each product was based on the same original GLODAP observations (Key et al., 2004). However, it is true that any OCIM deviations from real world circulation, errors in the empirical algorithms, or other errors in the assumptions inherent to the Carter et al. (2021) estimates would influence the preformed property estimates and contribute uncertainty to the magnitude of estimated OA metric changes caused by carbonate chemistry nonlinearities. To determine if data product incongruity is creating spurious results, we analyzed output from the CESM-ETHZ Global Ocean Biogeochemistry Model (GOBM; Doney, 2009; Lindsay et al., 2014; Yang & Gruber, 2016), which has internally consistent physics and chemistry, to confirm the contribution of carbonate system nonlinearities in driving subsurface OA metric changes. We relied on CESM-ETHZ model output in the Regional Carbon Cycle Assessment and Processes 2 archive (Müller, 2023) that extends from 1980 to 2018 and used two simulations that were forced with atmospheric reanalysis data: one with historically increasing CO_2 levels and one with constant, pre-industrial CO_2 levels. By differencing these simulations, we retrieved the C_{ant} distribution and calculated OA metric changes resulting from the accumulation of C_{ant}.

We focused our analysis on the year 2002 of model output for direct comparison with the observation-based assessment. To estimate the nonlinear component of OA metric changes in the GOBM data we need

the preformed property concentrations, which are not readily available. Therefore, we calculated the apparent oxygen utilization (AOU) and multiplied by the respiratory quotient (-170/117) to estimate the remineralized DIC concentration (DIC_{Org}). Without preformed total alkalinity and preformed nitrate values, we were unable to account for the calcium carbonate dissolution contribution to the total regenerated carbon pool; this proves to be unnecessary. We recalculated all OA metric values for the quasi-preformed ($DIC - DIC_{Org}$) and quasi-preformed preindustrial ($DIC - DIC_{Org} - C_{ant}$) ocean conditions. We also recalculated all OA metric values for the preindustrial ($DIC - C_{ant}$) ocean conditions. This allowed us to compare the impact of C_{ant} on OA metrics under (1) quasi-preformed versus (2) year 2002 ocean conditions and quantify the nonlinear component of OA metric changes in the model by difference (see Methods section). As discussed by Carter et al. (2021) and Cassar et al. (2021), AOU can overestimate true oxygen utilization due to the assumption of oxygen equilibrium between the atmosphere and surface ocean prior to water mass subduction. The DIC_{Org} values for the GOBM may therefore be overestimated. Our results indicate that the same sign and pattern of OA metric changes caused by carbonate system nonlinearities are occurring in the model and observational data products, suggesting that the combination of GLODAP-based data products is not causing spurious results that would alter our conclusions (**Figure S11**).

Text S3. ***Calculation of $[H^+]$ error from pH error***

For each grid cell:

$$[H^+]_1 = 10^{-pH}$$

$$[H^+]_2 = 10^{-(pH + pHerror)}$$

$$[H^+]_{error} = [H^+]_1 - [H^+]_2$$

Text S4. ***Calculation of in situ fCO_2***

CO2SYSv3 for MATLAB is based on earlier versions from Lewis & Wallace (1998), van Heuven et al. (2011), and Orr et al. (2018). Until recently, the CO2SYSv3 (Sharp et al., 2020) carbonate system calculator, among other versions of CO2SYS based on the original code of Lewis & Wallace (1998), did not include the pressure dependence of carbon dioxide gas (CO_2) solubility or the relationship between CO_2 fugacity (fCO_2) and partial pressure (Humphreys et al., 2022; Orr et al., 2015; Orr & Epitalon, 2015) (see equations below). Instead, output pCO_2 values reflected conditions at one atmosphere of pressure; the approximate pCO_2 if the water parcel were brought quasi-adiabatically to the sea surface ("quasi" because the calculations are performed with *in situ* temperature rather than potential temperature). Following the existing implementation of a pressure correction to the CO_2 solubility term within seacarb (Gattuso et al., 2020), a different carbonate system calculator, we modified the version of CO2SYSv3 used for this manuscript (v3.2.0) to account for hydrostatic pressure in addition to the non-ideal nature of CO_2 (**Figure**

S18) to compute the *in situ* fCO_2 values. An optional pressure correction for CO_2 solubility and the fugacity factor has very recently been implemented in CO2SYSv3 (v3.2.1), which produces identical results to our modified CO2SYSv3 code.

The equation to calculate $[CO_2]$ from fCO_2, with the pressure correction for the CO_2 solubility constant (K_0), is given below; where P is total pressure (atmospheric plus hydrostatic), $\bar{v}_{CO2}$ is the partial molal volume of CO_2, R is the ideal gas constant, and T is temperature in Kelvin (Weiss, 1974).

$$[\mathrm{CO_2}] = K_0 \, f\mathrm{CO_2} \exp[(1 - P)\,\overline{v}_{CO2}\, R\, T] \qquad \textbf{Eqn. S1}$$

The equation to convert between pCO_2 and fCO_2 is given below; where B is the virial coefficient of CO_2, x_2 is the sum of the mole fractions of gases other than CO_2, and $\delta_{12} = 57.7 - 0.188$ T (Weiss, 1974).

$$f\mathrm{CO_2} = p\mathrm{CO_2} \;\exp[(B + 2x_2^2\,\delta_{12})\,P/RT] \qquad \textbf{Eqn. S2}$$

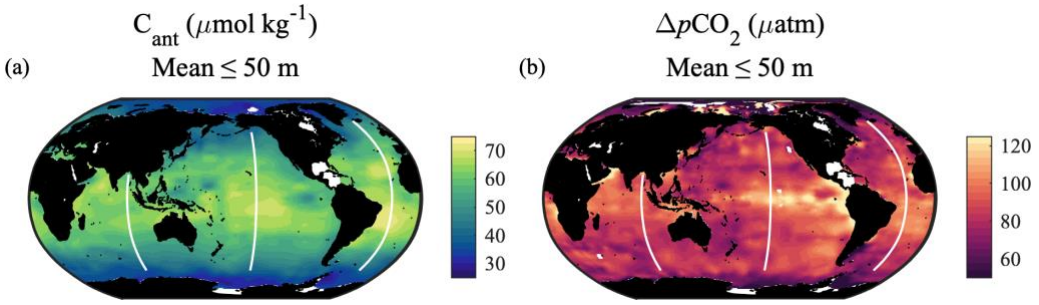

Figure S1. Average upper 50 m (**a**) anthropogenic carbon (C_{ant}) concentration in the year 2002 and (**b**) the change in carbon dioxide partial pressure (pCO_2) from the preindustrial period to the year 2002. White lines show key transects highlighted in subsequent figures. White patches reflect regions lacking data. Data (here and in subsequence figures, unless specified) are from the GLODAPv2.2016b mapped product (Lauvset et al., 2016).

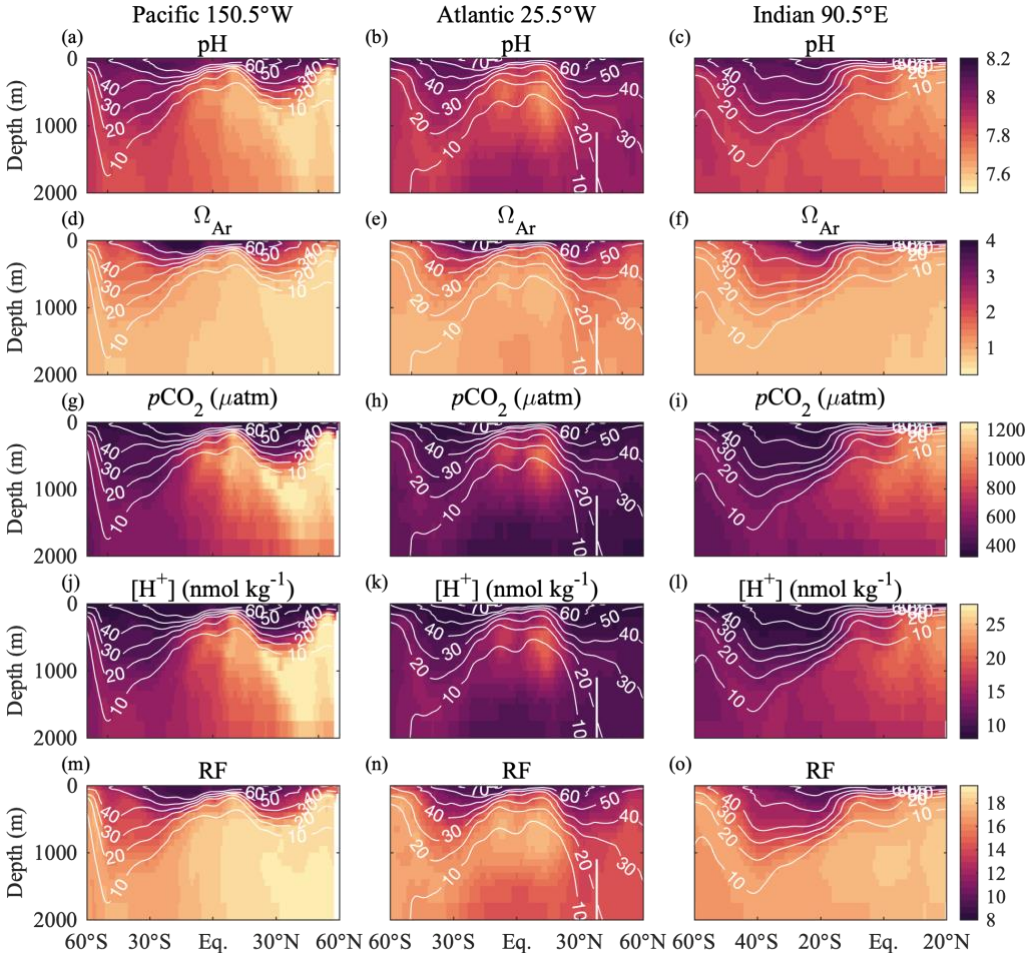

Figure S2. Year 2002 values of (**a-c**) pH, (**d-f**) aragonite saturation state (Ω_{Ar}), (**g-i**) pCO_2 (µatm), (**j-l**) [H^+] (nmol kg^{-1}), and the (**m-o**) Revelle sensitivity Factor (RF). Panels show data for the Pacific (150.5°W), Atlantic (25.5°W), and Indian (90.5°E) Oceans with meridional transect locations shown in Figure S1. White contours represent C_{ant} (µmol kg^{-1}) in the year 2002.

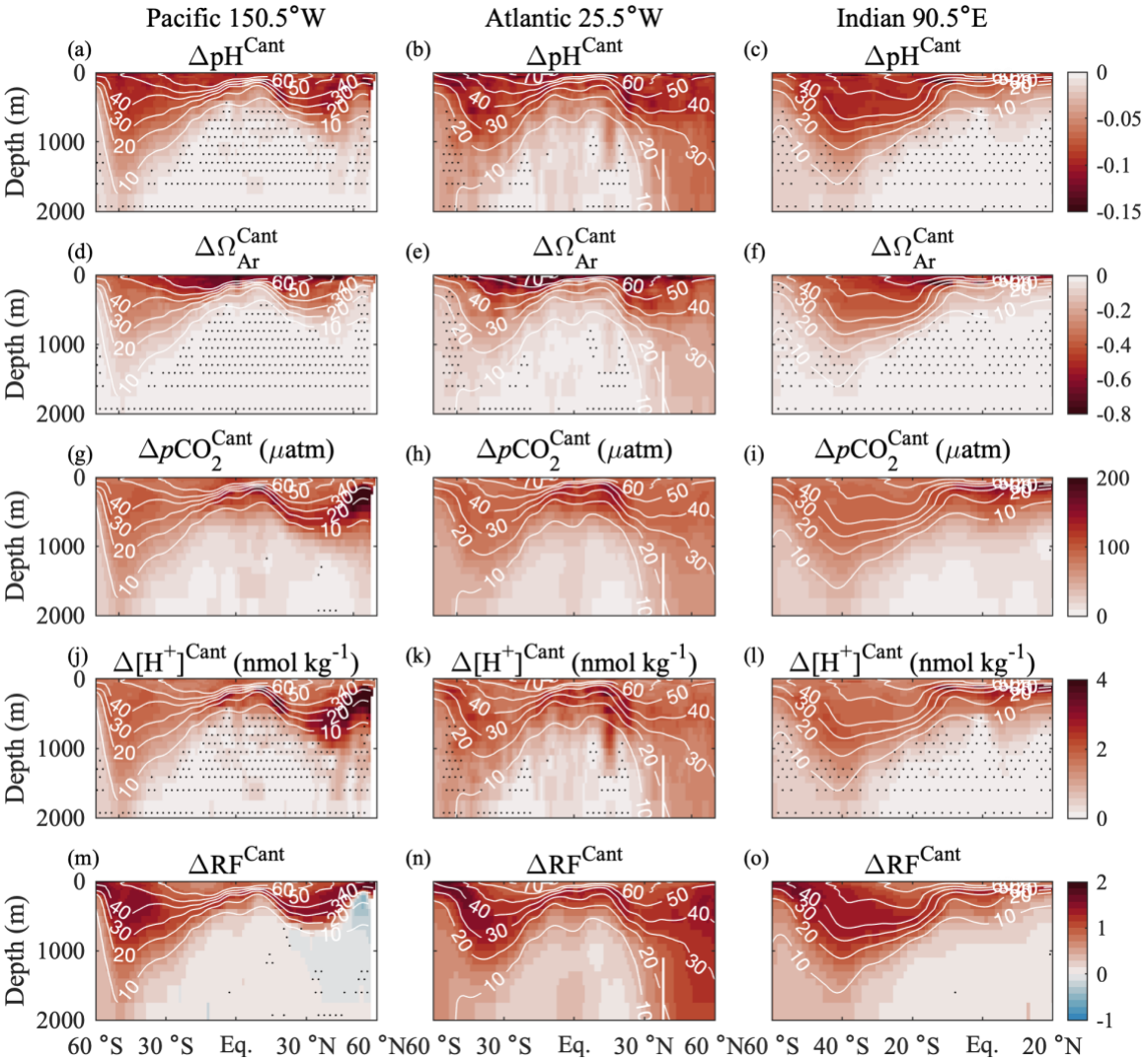

Figure S3. Changes (Δ) in (**a-c**) pH, (**d-f**) aragonite saturation state (Ω_{Ar}), (**g-i**) pCO_2 (μatm), (**j-l**) $[H^+]$ (nmol kg^{-1}), and the (**m-o**) Revelle sensitivity Factor (RF) due to the accumulation of C_{ant} (μmol kg^{-1}) since the preindustrial period. Panels show data for the Pacific (150.5°W), Atlantic (25.5°W), and Indian (90.5°E) Oceans with meridional transect locations shown in Figure S1. White contours represent C_{ant} (μmol kg^{-1}) in the year 2002. Black stippling shows where the magnitude of change is smaller than the propagated uncertainty.

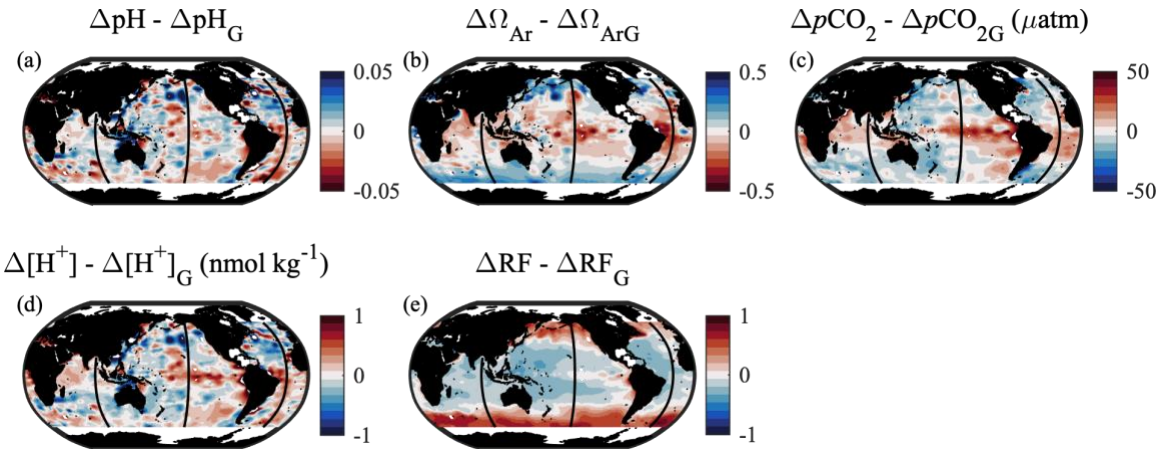

Figure S4. Local change (Δ) minus the global (computed from 60°S to 60°N) mean change (Δ_G) of each OA metric within the upper 50 m of the water column. Red (blue) areas indicate regions where the magnitude of the local change is larger (smaller) than the global mean change.

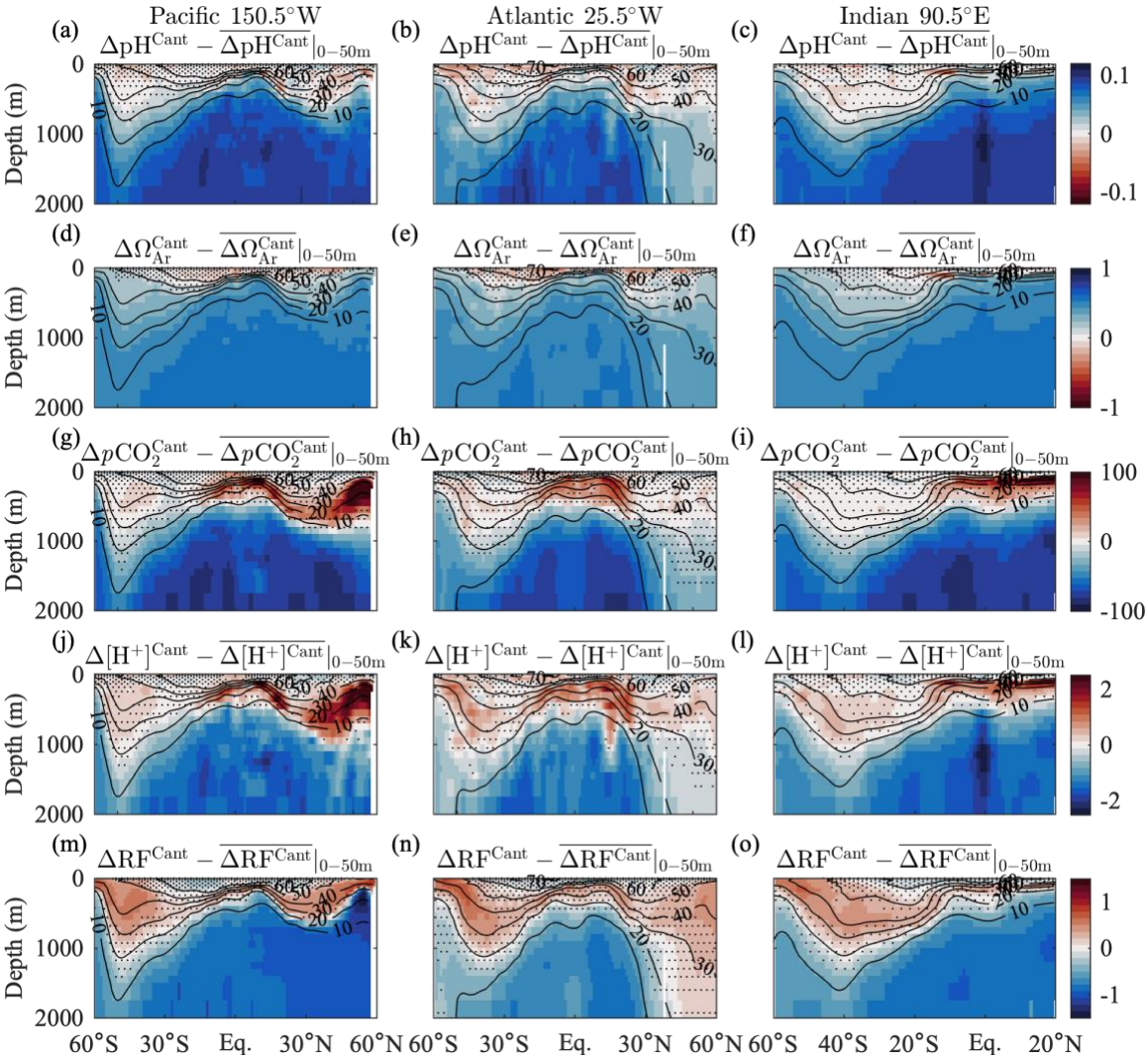

Figure S5. C_{ant}-induced OA metric changes (Δ), from the pre-industrial period to the year 2002, relative to the global (computed from 60°S to 60°N) mean change in the upper 50 m for (**a-c**) pH, (**d-f**) aragonite saturation state (Ω_{Ar}), (**g-i**) pCO_2 (µatm), (**j-l**) $[H^+]$ (nmol kg^{-1}), and the (**m-o**) Revelle sensitivity Factor (RF). Panels show data for the Pacific (150.5°W), Atlantic (25.5°W), and Indian (90.5°E) Oceans with meridional transect locations shown in Figure S1. Black contours represent C_{ant} (µmol kg^{-1}) in the year 2002. Red coloring indicates a subsurface change that is larger in magnitude than the global mean change in the upper 50 m. Stippling indicates where the magnitude of the change is smaller than the uncertainty.

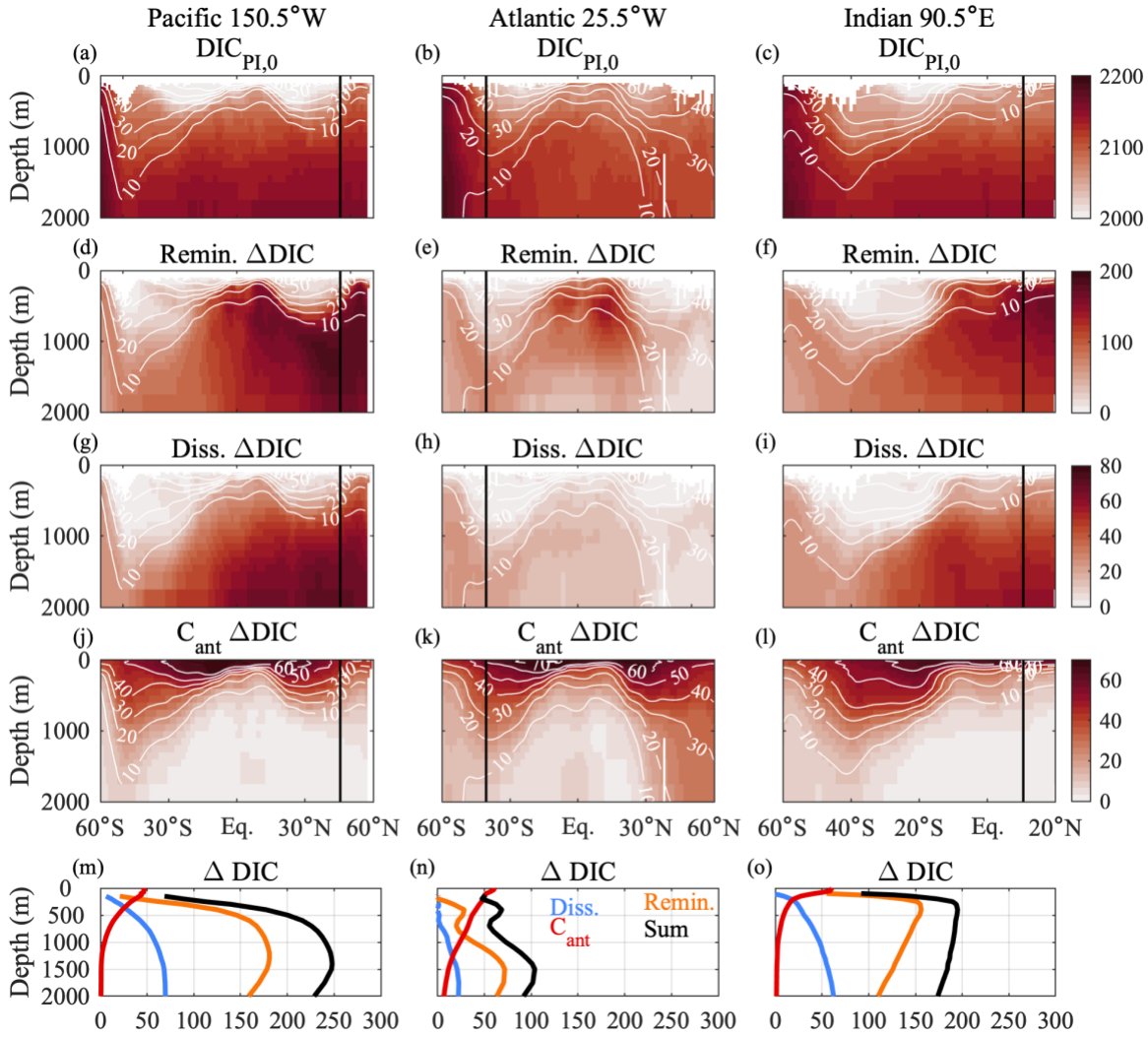

Figure S6. (**a-c**) Preindustrial preformed DIC ($DIC_{PI,0}$) and the impact on DIC (ΔDIC) of cumulative (**d-f**) remineralization (Remin.), (**g-i**) calcium carbonate dissolution (Diss.), and (**j-l**) anthropogenic carbon (C_{ant}) buildup. Panels show data for the Pacific (150.5°W), Atlantic (25.5°W), and Indian (90.5°E) Oceans with meridional transect locations shown in Figure S1. White contours represent C_{ant} (μmol kg^{-1}) in the year 2002. (**m-o**) Profiles of the DIC accumulated through each process at the latitudes indicated by black lines in above panels (45.5°N, 40.5°S, and 10.5°N). The sum of contributions (Sum) equals the difference between year 2002 DIC and $DIC_{PI,0}$. All panels show data in units of μmol kg^{-1}. Missing near surface values reflect waters considered to be in contact with the atmosphere, for which the preformed properties were not estimated by Carter et al., 2021.

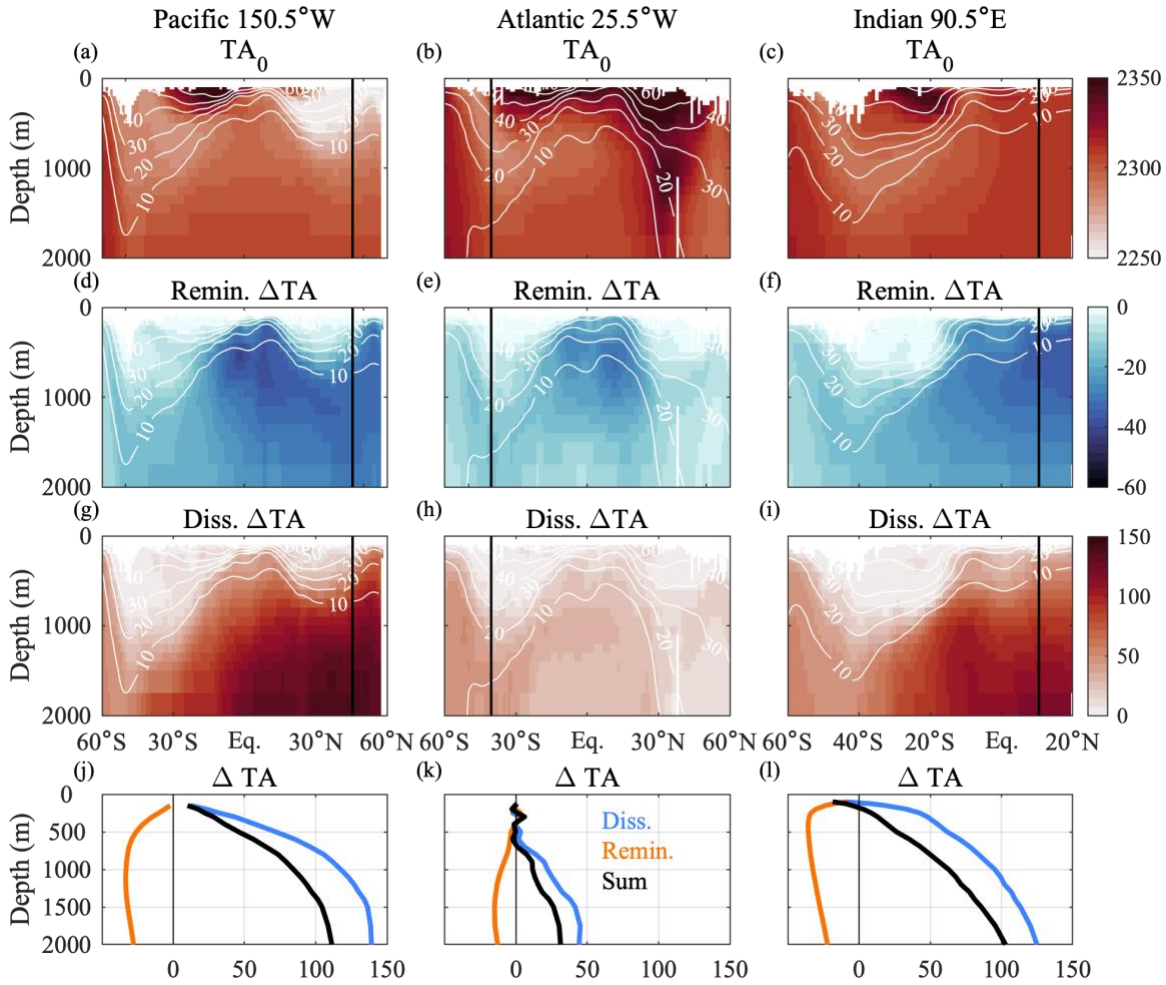

Figure S7. (**a-c**) Preformed TA (TA_0) and the impact on TA (ΔTA) of cumulative (**d-f**) remineralization (Remin.) and (**g-i**) calcium carbonate dissolution (Diss.). Panels show data for the Pacific (150.5°W), Atlantic (25.5°W), and Indian (90.5°E) Oceans with meridional transect locations shown in Figure S1. White contours represent C_{ant} (μmol kg^{-1}) in the year 2002. (**j-l**) Profiles of the TA accumulated through each process at the latitudes indicated by black lines in above panels (45.5°N, 40.5°S, and 10.5°N). The sum of contributions (Sum) equals the difference between year 2002 TA and TA_0. All panels show data in units of μmol kg^{-1}. Missing near surface values reflect waters considered to be in contact with the atmosphere, for which the preformed properties were not estimated by Carter et al., 2021.

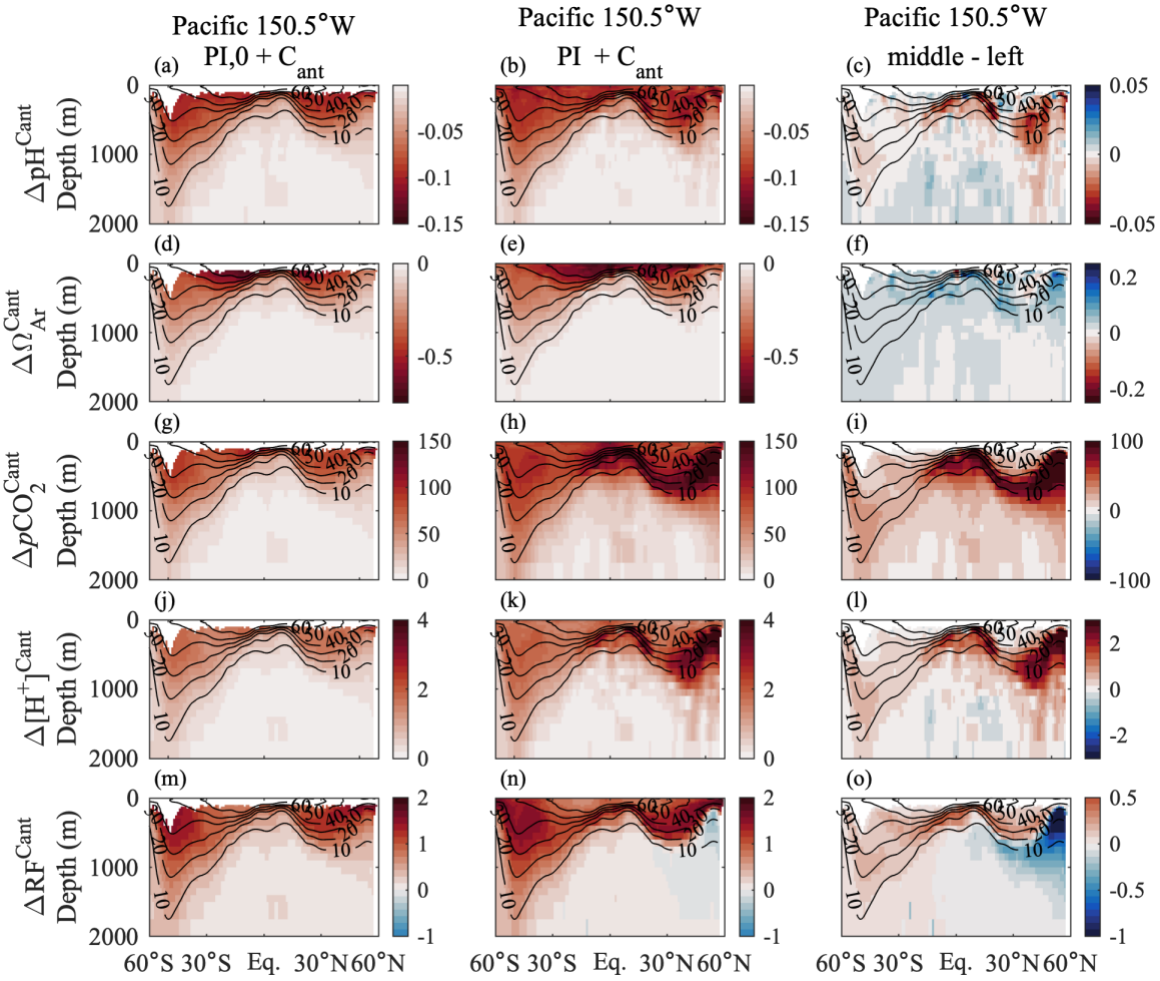

Figure S8. C_{ant}-induced OA metric changes (Δ) relative to the (**left**) preformed preindustrial (PI,0) conditions and (**middle**) preindustrial (PI) conditions and (**right**) the difference of the latter minus the former (also shown in **Figure 3**). Results are shown for (**a-c**) pH, (**d-f**) aragonite saturation state (Ω_{Ar}), (**g-i**) pCO_2 (µatm), (**j-l**) $[H^+]$ (nmol kg^{-1}), and the (**m-o**) Revelle sensitivity Factor (RF) in the Pacific Ocean (150.5°W). The meridional transect location is shown in Figure S1. Black contours represent C_{ant} (µmol kg^{-1}) in the year 2002. In the right column, red indicates nonlinear amplification and blue indicates nonlinear dampening of the OA metric change due to interactions between C_{ant} and natural carbon accumulated from organic matter remineralization and calcium carbonate dissolution.

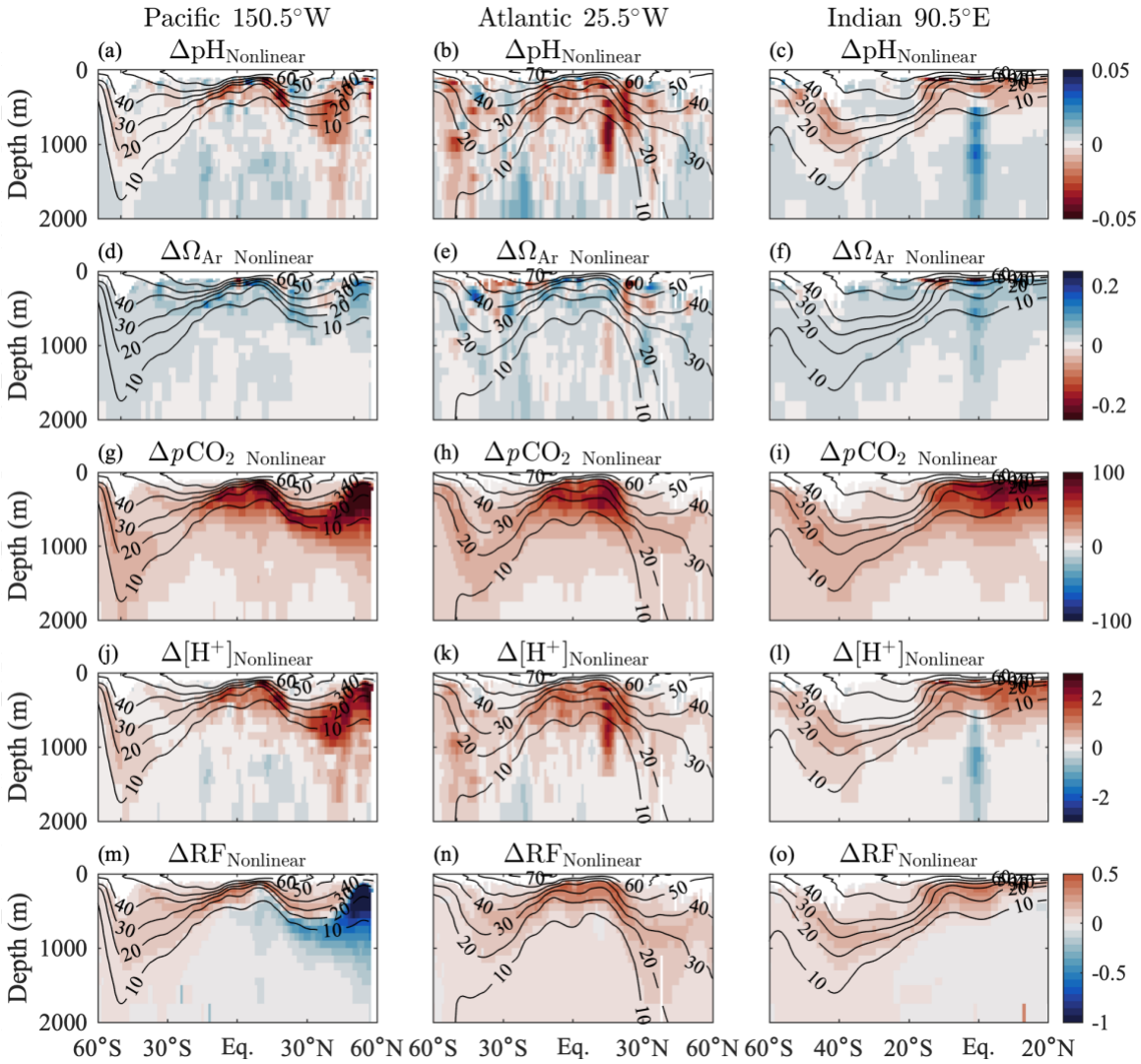

Figure S9. Nonlinear component of OA metric changes (Δ) caused by interactions between C_{ant} and natural carbon accumulated from organic matter remineralization and calcium carbonate dissolution when using a respiratory quotient of **0.7 × (-170/117)**. Red and blue coloring indicate where the OA metric responses to C_{ant} are amplified or dampened, respectively, by carbonate system nonlinearities resulting from carbon pool interactions. Results are shown for (**a-c**) pH (**d-f**) aragonite saturation state (Ω_{Ar}), (**g-i**) pCO_2 (µatm), (**j-l**) $[H^+]$ (nmol kg^{-1}), and (**m-o**) Revelle sensitivity Factor (RF). Black contours represent C_{ant} (µmol kg^{-1}) in the year 2002. Results for the Pacific (150.5°W), Atlantic (25.5°W), and Indian (90.5°E) Oceans with meridional transect locations shown in Figure 1a. Stippling indicates where the magnitude of the change is smaller than the uncertainty.

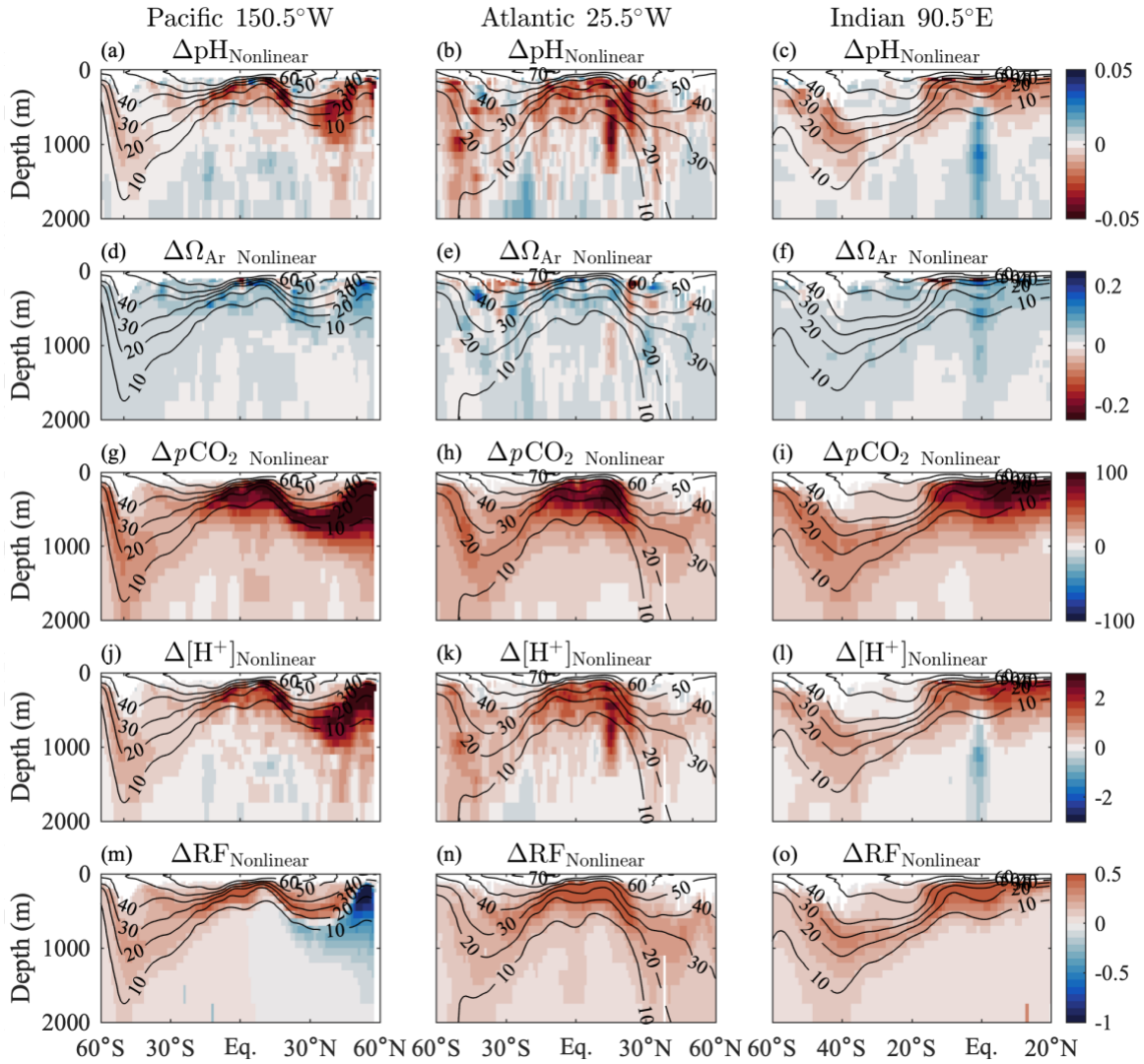

Figure S10. Nonlinear component of OA metric changes (Δ) caused by interactions between C_{ant} and natural carbon accumulated from organic matter remineralization and calcium carbonate dissolution when using a respiratory quotient of **1.3 × (-170/117)**. Red and blue coloring indicate where the OA metric responses to C_{ant} are amplified or dampened, respectively, by carbonate system nonlinearities resulting from carbon pool interactions. Results are shown for (**a-c**) pH (**d-f**) aragonite saturation state (Ω_{Ar}), (**g-i**) pCO_2 (µatm), (**j-l**) $[H^+]$ (nmol kg^{-1}), and (**m-o**) Revelle sensitivity Factor (RF). Black contours represent C_{ant} (µmol kg^{-1}) in the year 2002. Results for the Pacific (150.5°W), Atlantic (25.5°W), and Indian (90.5°E) Oceans with meridional transect locations shown in Figure 1a. Stippling indicates where the magnitude of the change is smaller than the uncertainty.

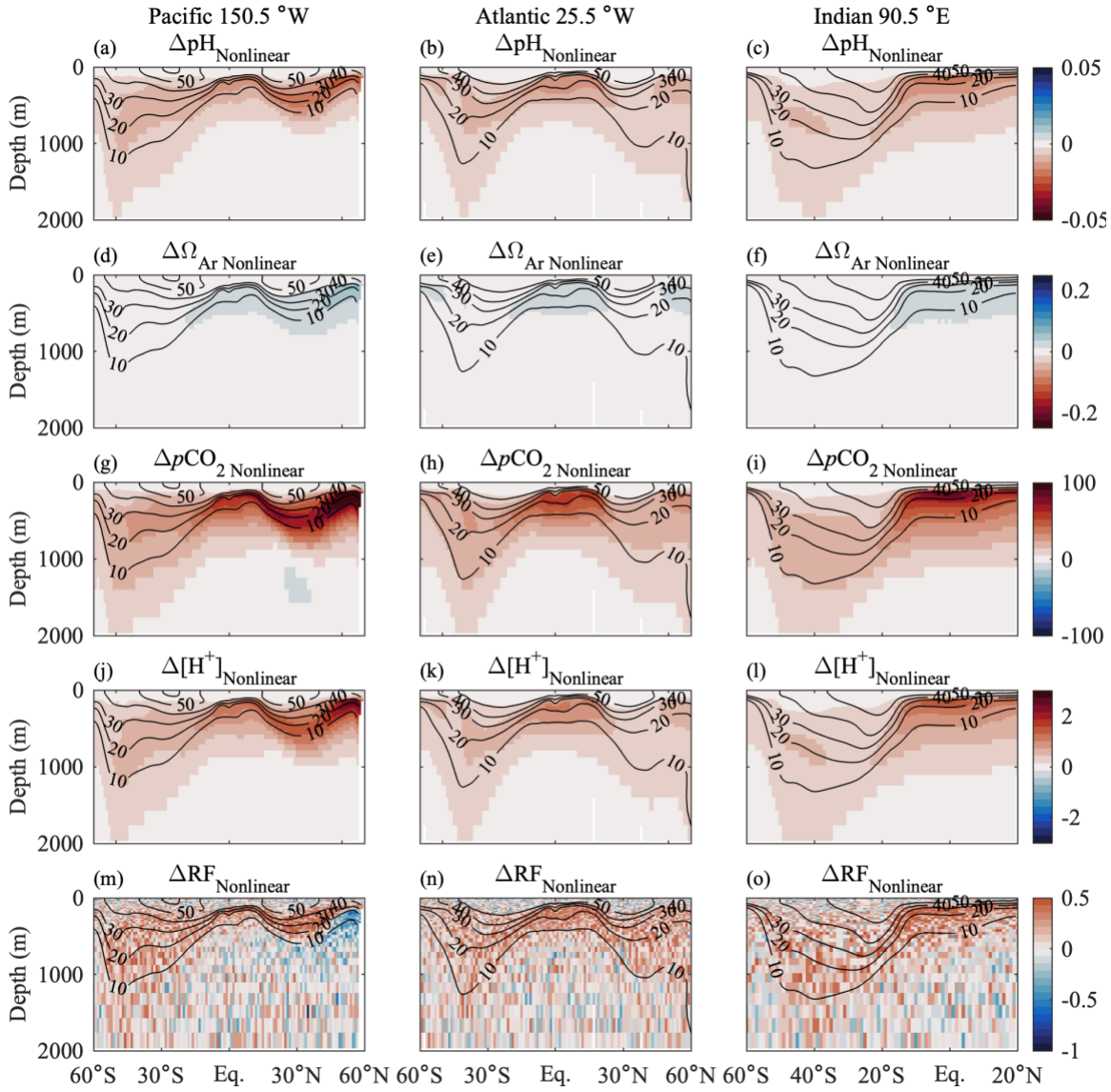

Figure S11. Nonlinear component of OA metric changes (Δ) caused by interactions between C_{ant} and natural carbon accumulated from organic matter remineralization based on year 2002 output from two simulations made with the CESM-ETHZ global ocean biogeochemistry model (details in **Text S2**). Red and blue coloring indicate where the OA metric responses to C_{ant} are amplified or dampened, respectively, by carbonate system nonlinearities resulting from carbon pool interactions. Results are shown for (**a-c**) pH (**d-f**) aragonite saturation state (Ω_{Ar}), (**g-i**) pCO_2 (µatm), (**j-l**) $[H^+]$ (nmol kg^{-1}), and (**m-o**) Revelle sensitivity Factor (RF). Black contours represent C_{ant} (µmol kg^{-1}) in the year 2002. Results for the Pacific (150.5°W), Atlantic (25.5°W), and Indian (90.5°E) Oceans with meridional transect locations shown in Figure 1a.

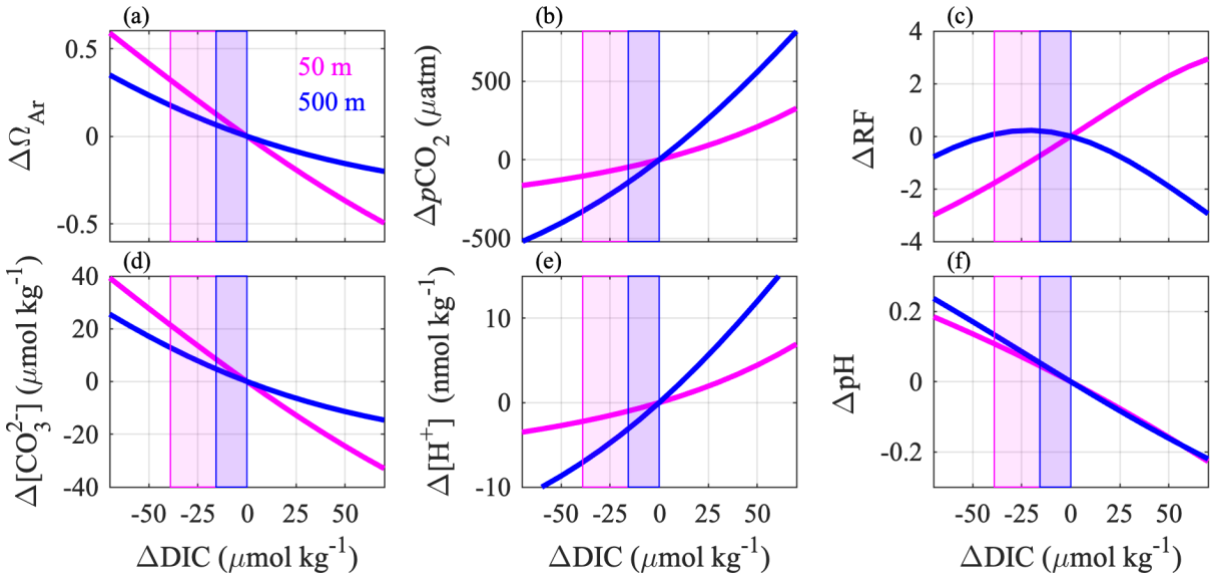

Figure S12. Changes in various OA metrics induced by adding or removing DIC from the 2002 DIC values at 50 m (pink line) and 500 m (blue line) depth for waters at 150.5°W and 45.5°N in the North Pacific Ocean. The shaded regions bound the OA metric changes that have occurred at each depth due to C_{ant}-accumulation from the preindustrial period through the year 2002, where ΔDIC = 0. The year 2002 DIC:TA ratios at 50 m and 500 m are 0.95 and 1.00, respectively (see **Figure S12**).

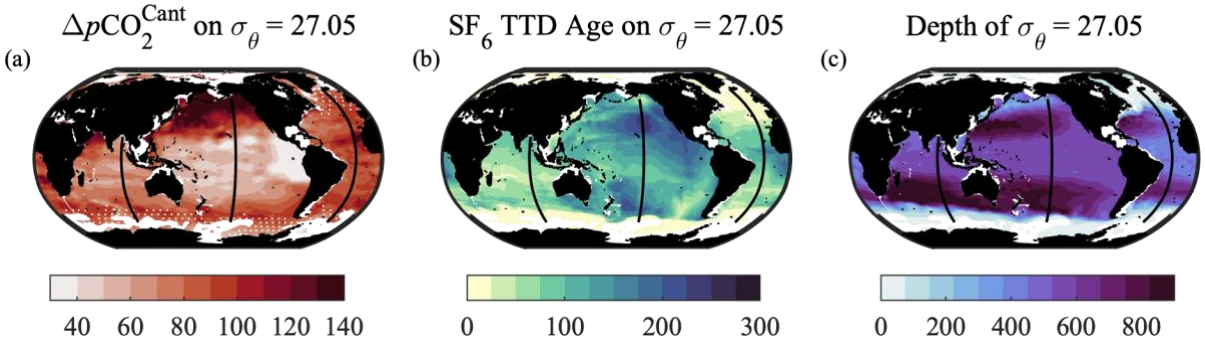

Figure S13. (**a**) C_{ant}-induced pCO_2 changes (μatm; Δ) since the preindustrial period on potential density surface (σ_θ) 27.05 kg m^{-3}. White stippling shows where the σ_θ = 27.05 kg m^{-3} surface is shallower than the maximum annual mixed layer depth based on a global ocean surface mixed layer statistical monthly climatology (GOSML 95th percentiles; Johnson & Lyman, 2022). (**b**) Mean age (years) of the σ_θ = 27.05 kg m^{-3} density surface based on data from Jeansson et al. (2021) that was linearly interpolated in three dimensions to fill gaps before extracting ages. Age was estimated using sulfur hexafluoride (SF_6) and the transient tracer distribution (TTD) method. (**c**) Depth (m) of the σ_θ = 27.05 kg m^{-3} density surface. White patches in all panels indicate areas with no data or where the potential density surface does not exist.

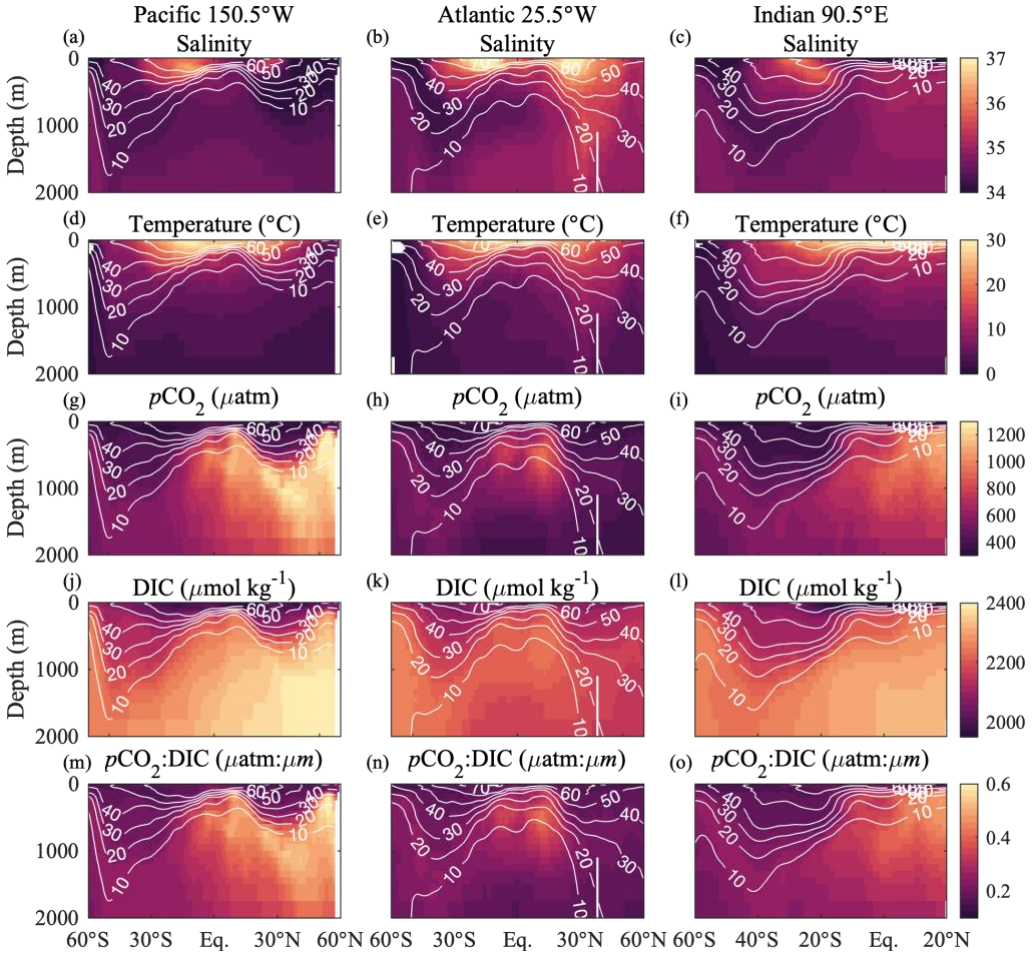

Figure S14. Year 2002 values of (**a-c**) salinity, (**d-f**) temperature, (**g-i**) pCO_2, (**j-l**) DIC, and (**m-o**) pCO_2:DIC ratio (μ*m* = μmol kg^{-1}). Panels show data for the Pacific (150.5°W), Atlantic (25.5°W), and Indian (90.5°E) Oceans with meridional transect locations shown in Figure S1. White contours represent C_{ant} (μmol kg^{-1}) in the year 2002.

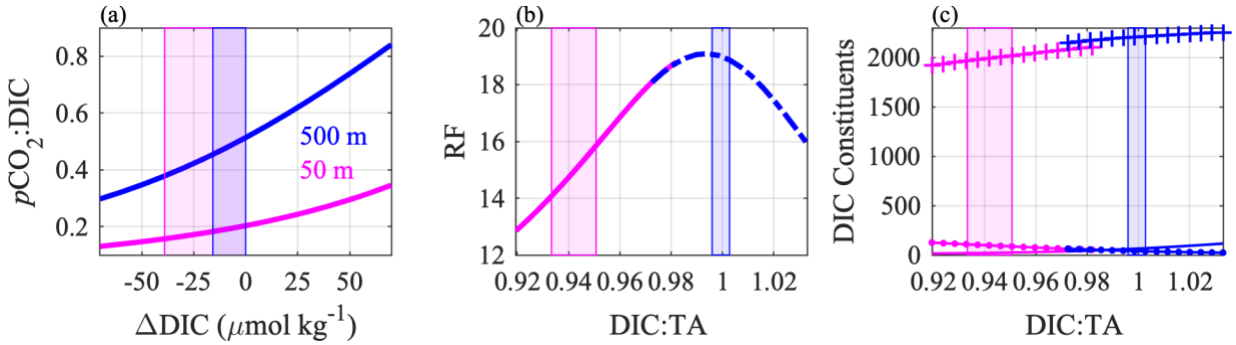

Figure S15. Change in the (**a**) pCO_2:DIC ratio (µatm : µmol kg^{-1}) (**b**) Revell sensitivity Factor (RF), and (**c**) concentration (µmol kg^{-1}) of aqueous CO_2 ([CO_2]), bicarbonate ion ([HCO_3^-]), and carbonate ion ([CO_3^{2-}]) induced by adding or removing DIC from the 2002 DIC values at 50 m (pink line) and 500 m (blue line) depth for waters at 150.5°W and 45.5°N in the North Pacific Ocean. The x-axis in subplot **a** shows the DIC change relative to the 2002 DIC values (ΔDIC) while the x-axes in subplots **b** and **c** show the DIC:TA ratios associated with the DIC changes. The shaded regions bound the OA metric changes that have occurred at each depth due to C_{ant}-accumulation through the year 2002, which is represented by the right edge of each shaded region in each panel.

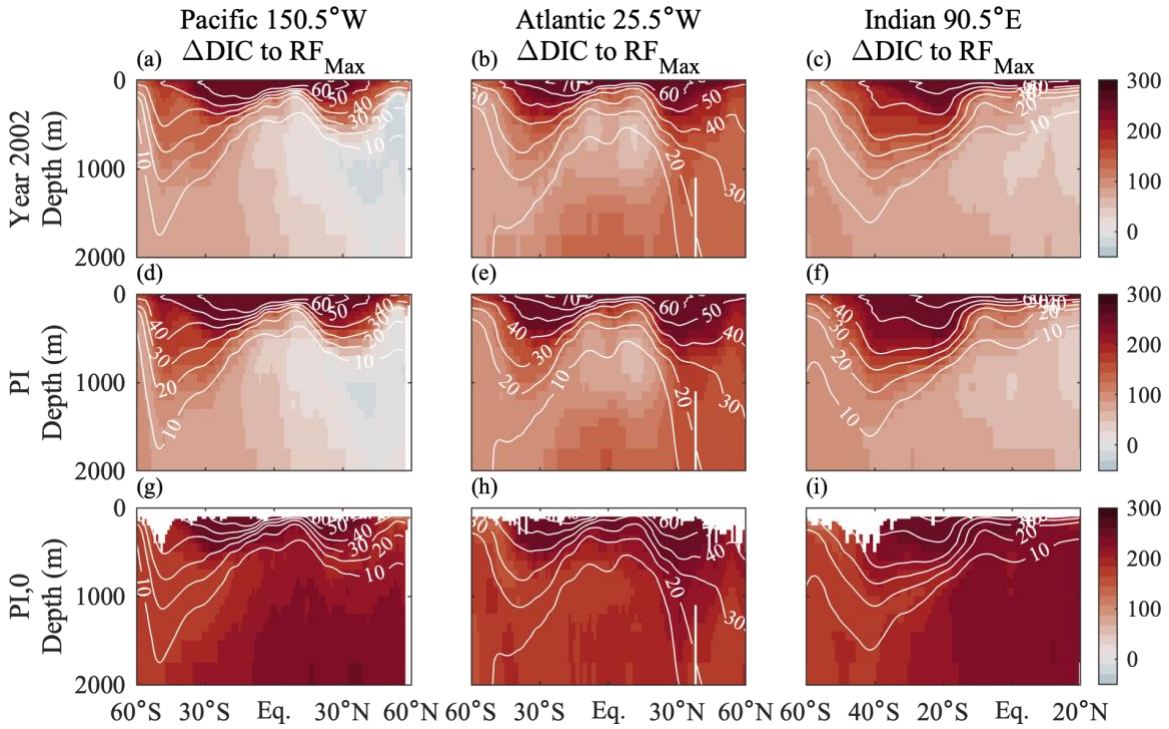

Figure S16. DIC addition (ΔDIC) required to reach the maximum RF value (RF_{Max}) when starting from DIC concentrations associated with (**a-c**) year 2002 conditions, (**d-f**) preindustrial (PI) conditions (including biological carbon byproducts), and (**g-i**) preformed preindustrial (PI,0) conditions (excluding biological carbon byproducts). Panels show data for the Pacific (150.5°W), Atlantic (25.5°W), and Indian (90.5°E) Oceans with meridional transect locations shown in Figure S1. White contours represent C_{ant} (μmol kg^{-1}) in the year 2002. Negative values indicate that DIC would need to be removed. Missing values in panels **g-i** reflect waters considered to be in contact with the atmosphere, for which the performed properties were not estimated by Carter et al., 2021.

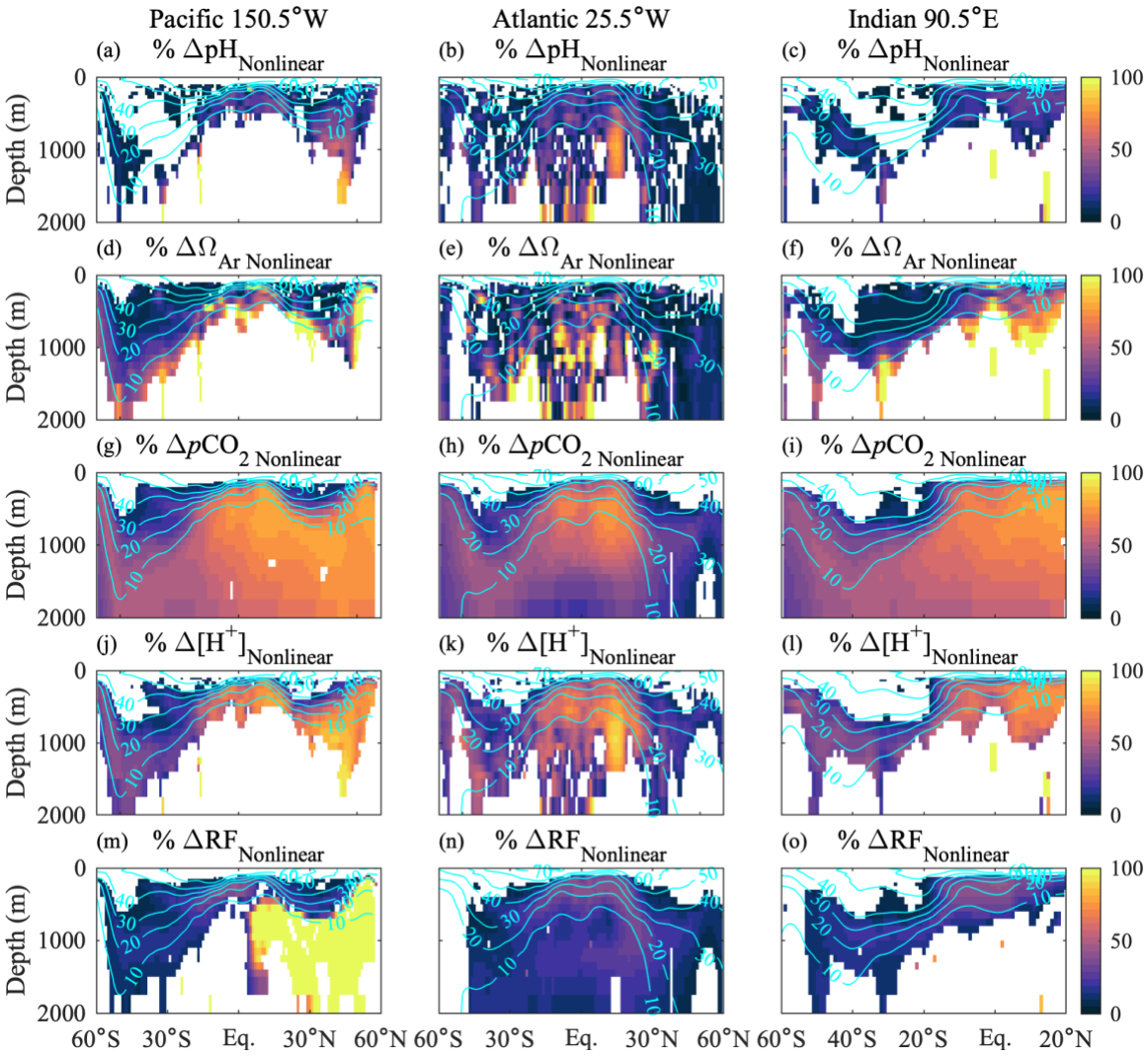

Figure S17. Absolute percent of the total C_{ant}-induced OA metric change (Δ), from the pre-industrial period to the year 2002, that is caused by carbonate system nonlinearities (NL) for (**a-c**) pH, (**d-f**) aragonite saturation state (Ω_{Ar}), (**g-i**) pCO_2 (µatm), (**j-l**) $[H^+]$ (nmol kg^{-1}), and the (**m-o**) Revelle sensitivity Factor (RF). Panels show data for the Pacific (150.5°W), Atlantic (25.5°W), and Indian (90.5°E) Oceans with meridional transect locations shown in Figure S1. Cyan contours represent C_{ant} (µmol kg^{-1}) in the year 2002. Estimates of the nonlinear and total component OA metric changes induced by C_{ant} that fell below their respective calculation uncertainties were excluded. The large nonlinear % contributions to Ω_{Ar} and pH that reside below the 10 µmol kg^{-1} C_{ant} contour are associated with very small $\Delta\Omega_{Ar}$ and ΔpH values, respectively (**Figure S3**).

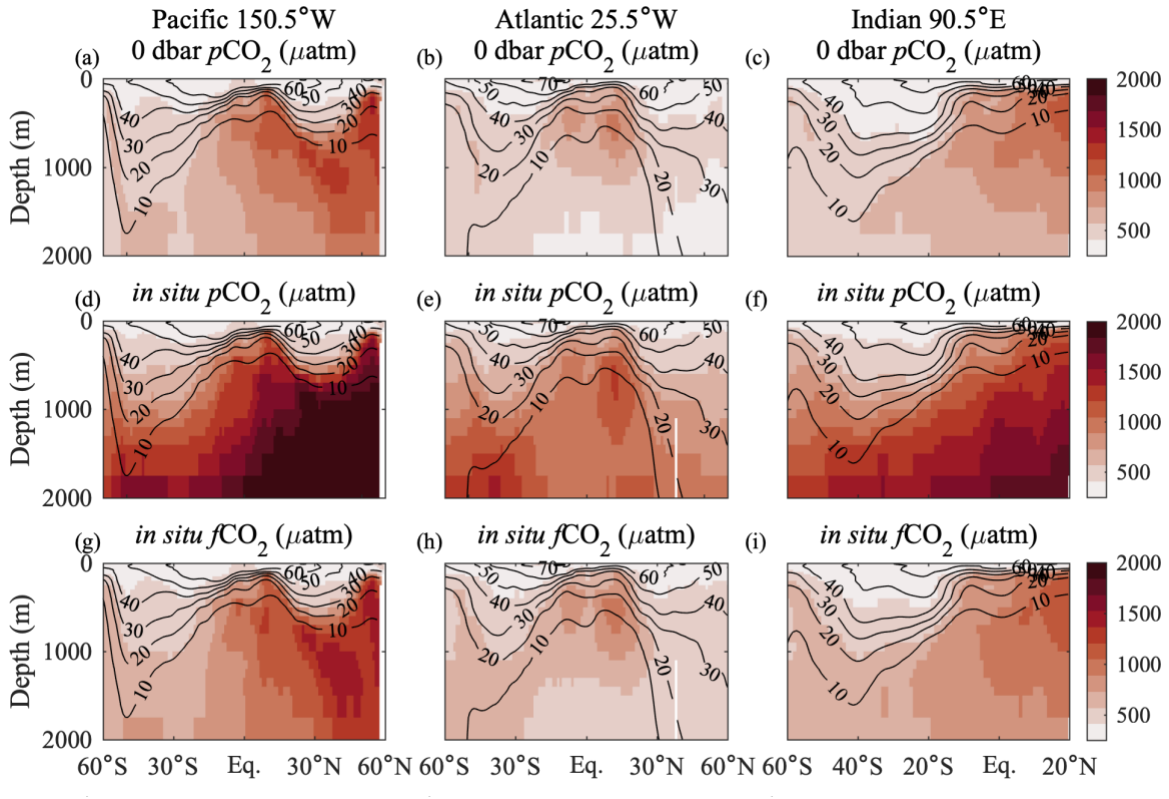

Figure S18. Examples of (**a-c**) pCO_2 at 0 decibars, (**d-f**) pCO_2 at *in situ* pressure, and (**g-i**) fCO_2 at *in situ* pressure, all in units of µatm. Panels show data for the Pacific (150.5°W), Atlantic (25.5°W), and Indian (90.5°E) Oceans with meridional transect locations shown in Figure S1. Black contours represent C_{ant} (µmol kg^{-1}) in the year 2002.

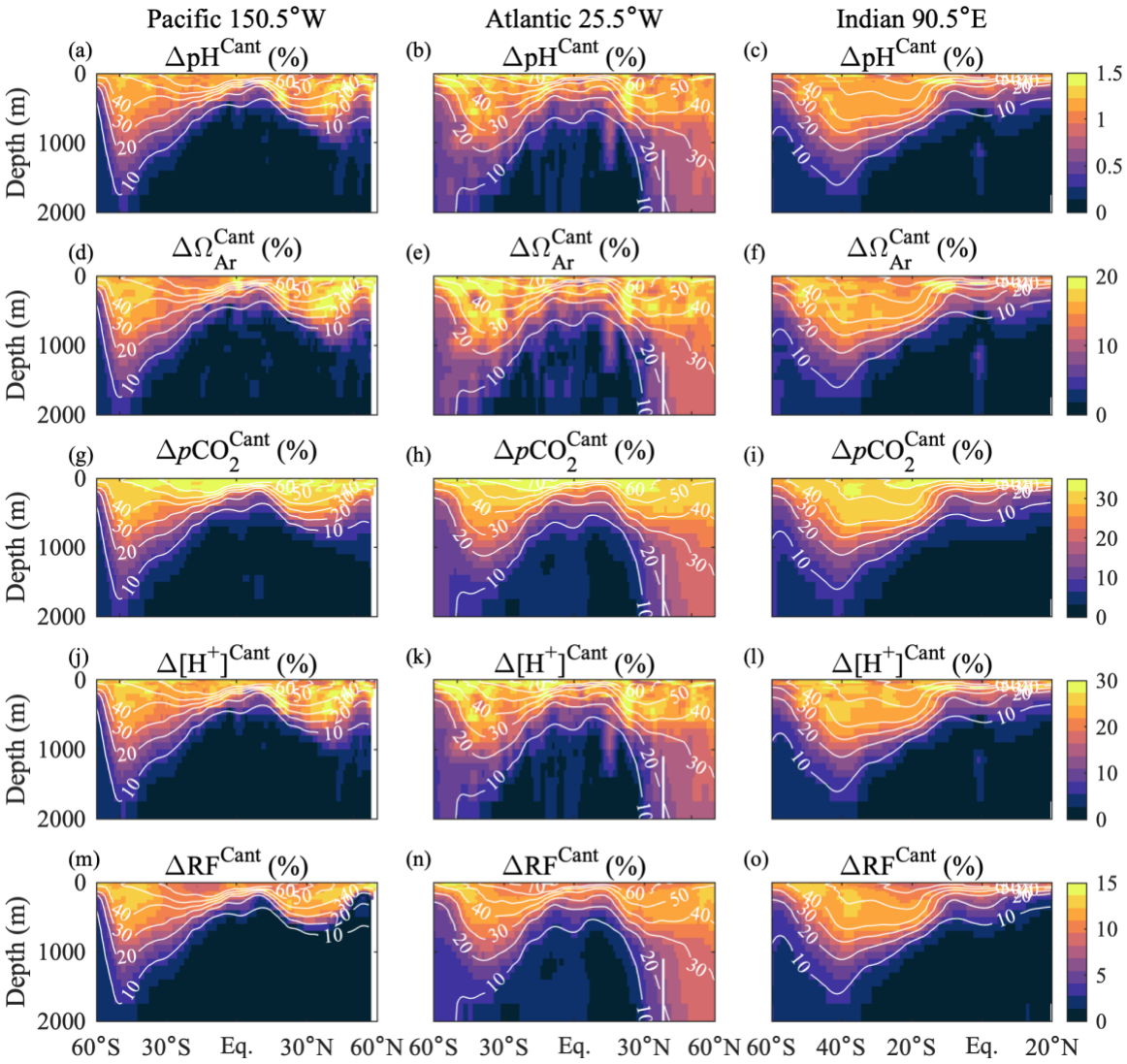

Figure S19. Magnitude of the C_{ant}-induced OA metric change (Δ), from the pre-industrial (PI) period to the year 2002, relative to the PI period value in terms of percent for (**a-c**) pH, (**d-f**) aragonite saturation state (Ω_{Ar}), (**g-i**) pCO_2 (µatm), (**j-l**) $[H^+]$ (nmol kg^{-1}), and the (**m-o**) Revelle sensitivity Factor (RF). Note the different color bar ranges for each OA metric. Panels show data for the Pacific (150.5°W), Atlantic (25.5°W), and Indian (90.5°E) Oceans with meridional transect locations shown in Figure S1. White contours represent C_{ant} (µmol kg^{-1}) in the year 2002.

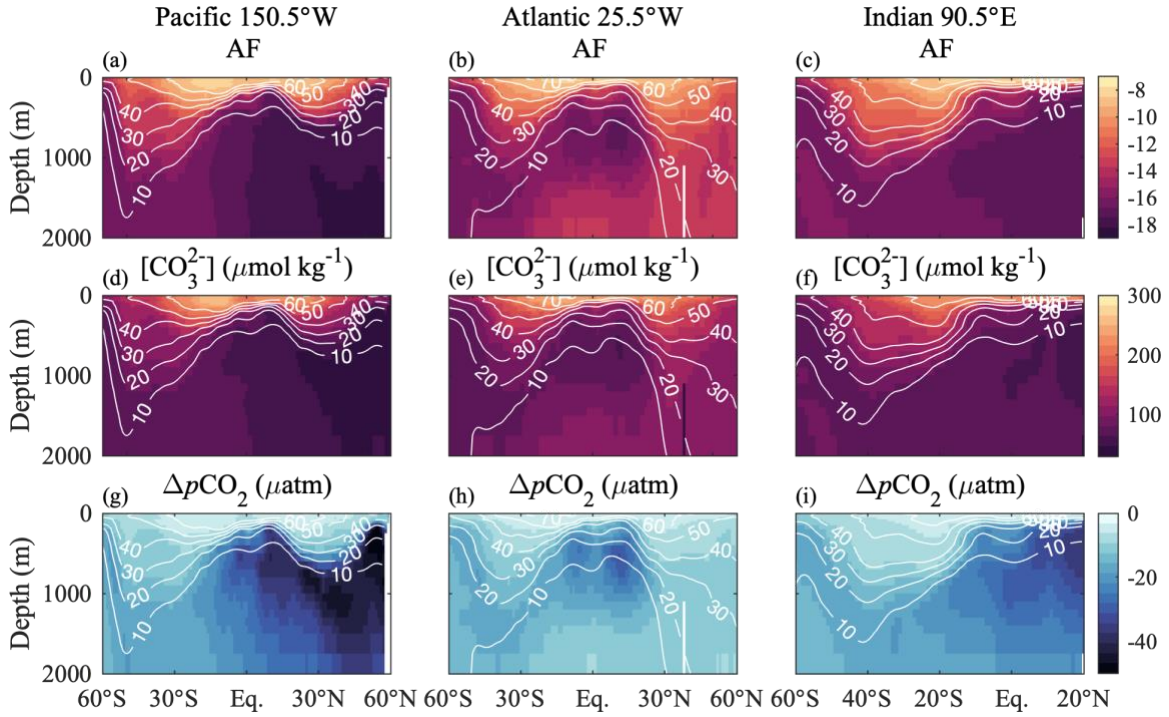

Figure S20. Year 2002 values of the (**a-c**) Alkalinity sensitivity Factor (AF) and (**d-f**) carbonate ion concentration [CO_3^{2-}], and the (**g-i**) pCO_2 change (Δ) associated with adding 5 μmol kg^{-1} DIC and 10 μmol kg^{-1} TA (mimicking hypothetical calcium carbonate dissolution) throughout the entire water column. Panels show data for the Pacific (150.5°W), Atlantic (25.5°W), and Indian (90.5°E) Oceans with meridional transect locations shown in Figure S1. White contours represent C_{ant} (μmol kg^{-1}) in the year 2002.

References

Carter, B. R., Feely, R. A., Lauvset, S. K., Olsen, A., DeVries, T., & Sonnerup, R. (2021). Preformed Properties for Marine Organic Matter and Carbonate Mineral Cycling Quantification. *Global Biogeochemical Cycles*, *35*(1). https://doi.org/10.1029/2020GB006623

Cassar, N., Nicholson, D., Khatiwala, S., & Cliff, E. (2021). Decomposing the Oxygen Signal in the Ocean Interior: Beyond Decomposing Organic Matter. *Geophysical Research Letters*, *48*(18), 1–12. https://doi.org/10.1029/2021GL092621

Doney, S. C. (2009). Mechanisms governing interannual variability in upper-ocean inorganic carbon system and air–sea CO_2 fluxes: Physical climate and atmospheric dust. *Deep Sea Research Part II: Topical Studies in Oceanography*, *56*(8–10), 640–655. https://doi.org/10.1016/j.dsr2.2008.12.006

Gattuso, J.-P., Epitalon, J.-M., & Orr, J. (2020). seacarb: Seawater Carbonate Chemistry (Version 3.2.13). Retrieved from https://CRAN.R-project.org/package=seacarb

Henderikx Freitas, F., White, A. E., & Quay, P. D. (2020). Diel Measurements of Oxygen- and Carbon-Based Ocean Metabolism Across a Trophic Gradient in the North Pacific. *Global Biogeochemical Cycles*, *34*(11), e2019GB006518. https://doi.org/10.1029/2019GB006518

van Heuven, S. M. A. C., Pierrot, D., Rae, J. W. B., Lewis, E., & Wallace, D. W. R. (2011). MATLAB program developed for CO_2 system calculations. *ORNL/CDIAC-105b. Carbon Dioxide Information Analysis Center, Oak Ridge National Laboratory, U.S. Department of Energy, Oak Ridge, Tennessee*. https://doi.org/10.3334/CDIAC/otg.CO2SYS_MATLAB_v1.1

Humphreys, M. P., Lewis, E. R., Sharp, J. D., & Pierrot, D. (2022). PyCO2SYS v1.8: marine carbonate system calculations in Python. *Geoscientific Model Development*, *15*(1), 15–43. https://doi.org/10.5194/gmd-15-15-2022

Jeansson, E., Steinfeldt, R., & Tanhua, T. (2021). Water mass ages based on GLODAPv2 data product (NCEI Accession 0226793). Mean age calculated from SF6 and the TTD method in years. NOAA National Centers for Environmental Information. Retrieved from https://doi.org/10.25921/xp33-q351

Johnson, G. C., & Lyman, J. M. (2022). GOSML: A Global Ocean Surface Mixed Layer Statistical Monthly Climatology: Means, Percentiles, Skewness, and Kurtosis. *Journal of Geophysical Research: Oceans*, *127*. https://doi.org/10.1029/2021JC018219

Lauvset, S. K., Key, R. M., Olsen, A., van Heuven, S. M. A. C., Velo, A., Lin, X., et al. (2016). A new global interior ocean mapped climatology: the 1° × 1° GLODAP version 2. *Earth System Science Data*, *8*(2), 325–340. https://doi.org/10.5194/essd-8-325-2016

Lewis, E., & Wallace, D. W. R. (1998). Program developed for CO_2 system calculations. *Carbon Dioxide Information Analysis Center, Oak Ridge National Laboratory, U.S. Department of Energy, Oak Ridge, Tennessee. Environmental Sciences Division. Publication No. 4735*. Oak Ridge TN, Oak Ridge National Laboratory Environmental Sciences Division, v. 4735. https://doi.org/4735

Lindsay, K., Bonan, G. B., Doney, S. C., Hoffman, F. M., Lawrence, D. M., Long, M. C., et al. (2014). Preindustrial-Control and Twentieth-Century Carbon Cycle Experiments with the Earth System Model CESM1(BGC). *Journal of Climate*, *27*(24), 8981–9005. https://doi.org/10.1175/JCLI-D-12-00565.1

Moreno, A. R., Garcia, C. A., Larkin, A. A., Lee, J. A., Wang, W., Moore, J. K., et al. (2020). Latitudinal gradient in the respiration quotient and the implications for ocean oxygen availability. *Proceedings of the National Academy of Sciences*, 202004986. https://doi.org/10.1073/pnas.2004986117

Moreno, A. R., Larkin, A. A., Lee, J. A., Gerace, S. D., Tarran, G. A., & Martiny, A. C. (2022). Regulation of the Respiration Quotient Across Ocean Basins. *AGU Advances*, *3*(5), e2022AV000679. https://doi.org/10.1029/2022AV000679

Müller, J. D. (2023). RECCAP2-ocean data collection [Data set]. Zenodo. https://doi.org/10.5281/zenodo.7990823

Orr, J. C., & Epitalon, J. M. (2015). Improved routines to model the ocean carbonate system: Mocsy 2.0. *Geoscientific Model Development*, *8*(3), 485–499. https://doi.org/10.5194/gmd-8-485-2015

Orr, J. C., Epitalon, J.-M., & Gattuso, J.-P. (2015). Comparison of ten packages that compute ocean carbonate chemistry. *Biogeosciences*, *12*(5), 1483–1510. https://doi.org/10.5194/bg-12-1483-2015

Orr, James C., Epitalon, J.-M., Dickson, A. G., & Gattuso, J.-P. (2018). Routine uncertainty propagation for the marine carbon dioxide system. *Marine Chemistry*, *207*(October), 84–107. https://doi.org/10.1016/j.marchem.2018.10.006

Sharp, J. D., Pierrot, D., Humphreys, M. P., Epitalon, jean-M., Orr, J. C., Lewis, E. R., & Wallace, D. W. R. (2020). CO2SYSv3 for MATLAB. Retrieved from https://doi.org/10.5281/zenodo.4023039

Weiss, R. F. (1974). Carbon dioxide in water and seawater: the solubility of a non-ideal gas. *Marine Chemistry*, *2*(3), 203–215. https://doi.org/10.1016/0304-4203(74)90015-2

Yang, S., & Gruber, N. (2016). The anthropogenic perturbation of the marine nitrogen cycle by atmospheric deposition: Nitrogen cycle feedbacks and the 15N Haber-Bosch effect. *Global Biogeochemical Cycles*, *30*(10), 1418–1440. https://doi.org/10.1002/2016GB005421